Atmos. Meas. Tech. Discuss., doi:10.5194/amt-2017-31, 2017
Manuscript under review for journal Atmos. Meas. Tech.
Discussion started: 27 February 2017

Atmospheric Measurement Techniques Discussions

An Assessment of the Impact of ATMS and CrIS Data Assimilation on Precipitation Prediction over the Tibetan Plateau

Tong Xue

Key Laboratory of China Education Ministry for Meteorological Disasters, Nanjing University of Information Science and Technology, Nanjing, China

Guangdong Ocean University, Zhanjiang, China

Jianjun Xu

Guangdong Ocean University, Zhanjiang, China,

GENRI, College of Science, George Mason University, Fairfax, Virginia, USA

Zhaoyong Guan

Nanjing University of Information Science and Technology, Nanjing, China

Long S. Chiu

AOES, College of Science, George Mason University, Fairfax, Virginia, USA,

Han-Ching Chen

Department of Atmospheric Sciences, National Taiwan University, Taipei, Taiwan

Min Shao

GENRI, College of Science, George Mason University, Fairfax, Virginia, USA

*Corresponding author contact information: Dr. JIANJUN XU, Guangdong Ocean University, Zhanjiang, China. Email: jxu14@gmu.edu

Atmos. Meas. Tech. Discuss., doi:10.5194/amt-2017-31, 2017
Manuscript under review for journal Atmos. Meas. Tech.
Discussion started: 27 February 2017

Atmospheric Measurement Techniques Discussions

Abstract

Using the National Oceanic and Atmospheric Administration's Gridpoint Statistical Interpolation data assimilation system and the National Center for Atmospheric Research's Advanced Research Weather Research and Forecasting (WRF-ARW) regional model, the impact of assimilating advanced technology microwave sounder (ATMS) and cross-track infrared sounder (CrIS) satellite data on precipitation prediction over the Tibetan Plateau in July 2015 was evaluated. Four experiments were designed: a control experiment and three data assimilation experiments with different data sets injected: conventional data only, a combination of conventional and ATMS satellite data, and a combination of conventional and CrIS satellite data. The results showed that the monthly mean of precipitation is shifted northward in the simulations and shows an orographic bias described as an overestimation in the upwind of the mountains and an underestimation in the south of the rainbelt. The rain shadow mainly influenced prediction of the quantity of precipitation, although the main rainfall pattern was well simulated. For the first 24-hourand last 24-hour accumulated daily precipitation, the model generally overestimated the amount of precipitation, but it was underestimated in the heavy rainfall periods of 3-6, 13-16, and 22-25 July. The observed water vapor conveyance from the southeastern Tibetan Plateau was larger than in the model simulations, which induced inaccuracies in the forecast of heavy rain on 3–6 July. The data assimilation experiments, particularly the ATMS assimilation, were closer to the observations for the heavy rainfall process than the control. Overall, the satellite data assimilation can enhance the

Atmos. Meas. Tech. Discuss., doi:10.5194/amt-2017-31, 2017
Manuscript under review for journal Atmos. Meas. Tech.
Discussion started: 27 February 2017

Atmospheric Measurement Techniques Discussions

WRF-ARW model's ability to predict the spatial and temporal pattern of precipitation in July 2015 although the model capability exists a significant limitation in the complex terrain area.

Key words: Radiance data assimilation, GSI, Tibetan Plateau, Weather forecast accuracy

Atmos. Meas. Tech. Discuss., doi:10.5194/amt-2017-31, 2017
Manuscript under review for journal Atmos. Meas. Tech.
Discussion started: 27 February 2017

Atmospheric Measurement Techniques Discussions

1. Introduction

The Tibetan Plateau (TP) is the highest and largest plateau in the world. It is located in the central Eurasian continent and stands in the middle troposphere, covering an area of approximately 2.5 million km^2. The TP has a variety of topographical features of a large terrain gradient and its steep mountains are aligned with an east-to-west arrangement. The dramatic modification caused by the rugged terrain influence the local atmospheric circulation and cause strong local convection to arise, easily inducing severe weather such as heavy rainfall, windstorms, hailstorms, and so on (Massacand et al., 1998; Gao et al., 2015). Precipitation is one of the key variables for understanding the hydrological cycle on the TP and has profound effects on the regional and global circulation that affect millions of people in the adjacent areas (Ye and Gao, 1979; Chen et al., 1985; Chambon et al., 2014; Li et al., 2014). Therefore, making accurate and long-lead weather forecasts at high temporal and spatial resolution for the TP not only has scientific significance but also addresses the urgent need for disaster prevention. However, due to the variable weather conditions and complex terrain orography, the TP remains a sparsely populated region with few conventional observation data sources, and the limited available meteorological data leads to great uncertainties in the regional weather forecasts. The continuous development of numerical weather prediction (NWP) models, such as the National Center for Atmospheric Research (NCAR)'s Advanced Research Weather and Research Forecasting (WRF-ARW) model, offer opportunities to improve regional weather forecasts in data-sparse regions. NWP models can be initialized with and laterally assimilate observation data, which is beneficial for better describing atmospheric conditions, thus

Atmos. Meas. Tech. Discuss., doi:10.5194/amt-2017-31, 2017
Manuscript under review for journal Atmos. Meas. Tech.
Discussion started: 27 February 2017

Atmospheric Measurement Techniques Discussions

keeping model results close to observations (Maussion et al., 2011).

Satellite radiance data are one of the most important observation data sources and can be directly assimilated into data assimilation models. Compared with conventional observation data, geostationary satellite data have continuous spatial and temporal coverage and polar orbiting satellites circle the earth twice a day to provide global observations of multiple meteorological variables, such as temperature, pressure, moisture, and so on. Moreover, many studies have suggested that the assimilation of satellite radiance data can substantially improve weather forecasts (Eyre, 1992; Derber and Wu, 1998; Xu et al., 2009). For longer-range prediction, satellite data are even more crucial than conventional observations (Zapotocny et al., 2008), Past studies have also indicated that the effect of assimilation of both observations and satellite products was better than only satellite data assimilation (Liu et al., 2013).However, the performance of satellite radiance assimilation in limited-area modeling systems using variational DA method is still controversial (Zou et al., 2013; Newman et al., 2015).Schwartz et al. (2012) was the first to assimilate microwave radiances with the region lacking observation stations using ensemble Kalman filter (ENKF) and the results showed that assimilating microwave radiances overall make better forecasts of Typhoon Morakot (2009). The negative influence has also appeared and it is mainly contributed to various of factors such as the influence of lateral boundary conditions within the regional domain (Warner et al., 1997) and non-uniform satellite coverage (Kazumori et al., 2013). .

The advanced technology microwave sounder (ATMS) and cross-track infrared sounder (CrIS)

Atmos. Meas. Tech. Discuss., doi:10.5194/amt-2017-31, 2017
Manuscript under review for journal Atmos. Meas. Tech.
Discussion started: 27 February 2017

Atmospheric Measurement Techniques Discussions

are two instruments with high resolution onboard the Suomi National Polar-orbiting Partnership spacecraft , a polar-orbiting satellite launched in 2011 with the aim to provide real-time sensor data for critical weather and climate measurements. The ATMS, a cross-track microwave scanner with 22 channels, combines most of the channels of the preceding advanced microwave sounding unit (AMSU-A) and microwave humidity sounder (MHS) to provide sounding profiles of atmospheric moisture and temperature. The CrIS is a Fourier transform spectrometer with 1305 spectral channels inherited from the high-resolution infrared radiation sounder (HIRS) to produce temperature, pressure, and moisture profiles. A previous study assimilated ATMS data in the European Centre for Medium-Range Weather Forecasts system and the results showed that the instrument has better performance than AMSU-A and MHS in the longer range over the Northern Hemisphere (Bormann et al., 2013). Nevertheless, satellite data assimilation into NWP models over the TP presents special challenges, because the limited model capability for assimilating radiance data over complex terrain with heterogeneous characteristics is still not clearly recognized. Furthermore, whether the new generation of satellite observations, such as ATMS and CrIS, can compensate for the shortage of data over the TP and effectively enhance the accuracy of forecasts remains unknown.

In this paper, we make an assessment of the impact of assimilating ATMS and CrIS radiance data for East Asia on precipitation prediction over the TP and compare the effects of different satellite data sets injected.

2. Data and Models

Atmos. Meas. Tech. Discuss., doi:10.5194/amt-2017-31, 2017
Manuscript under review for journal Atmos. Meas. Tech.
Discussion started: 27 February 2017

Atmospheric Measurement Techniques Discussions

107 *2.1 Data*

108 *2.1.1 Background data*

109 The National Centers for Environmental Prediction (NCEP) global forecast system (GFS)
110 forecast data, which has a horizontal resolution of 0.5° × 0.5° with a 6-hour interval, were used as
111 the boundary and initial conditions for the control (CTRL) experiment, while the background fields
112 of data assimilation experiments (DA) take advantages of the forecast product at 0600 UTC made
113 by CTRL. The GFS data is publicly available from https://www.ncdc.noaa.gov/data-access/model-
114 data/model-datasets/global-forcast-system-gfs.

115

116 *2.1.2 Observation data*

117 Observational precipitation data from the National Meteorological Information Center (NMIC)
118 of the China Meteorological Administration (CMA) was used as the truth data for comparison with
119 the model results. The 0.1° × 0.1° high-resolution gridded hourly China Merged Precipitation
120 Analysis (CMPA) data gauge, which combines the CMA's rain gauge hourly data provided by
121 more than 30,000 automatic weather stations with the National Oceanic and Atmospheric
122 Administration (NOAA) Climate Prediction Center's Morphing (CMORPH) precipitation product
123 (Xie & Xiong, 2011; Pan et al., 2012; Shen et al., 2014), was used for verification to evaluate the
124 model simulation results. Previous study (Guo et al., 2014) have compared the CMORPH data
125 with other data sets in the TP area. Considering the topographically complex terrain characterizing
126 the TP, satellite precipitation data with very high spatial resolution is especially needed. Of the

Atmos. Meas. Tech. Discuss., doi:10.5194/amt-2017-31, 2017
Manuscript under review for journal Atmos. Meas. Tech.
Discussion started: 27 February 2017

Atmospheric Measurement Techniques Discussions

Several merged satellite precipitation products (i.e.TMPA, PERSIANN, and GSMaP), the CMORPH product has the highest resolution (8 km) and so it is the most suitable product to use in studying precipitation patterns over the TP (Guo et al.,2014). The spatiotemporal resolution of CMORPH products is also considerably higher than that of TRMM 3B42 products. Past study has also made a conclusion that the high resolution CMORPH data can depict finer regional details, such as a less coherent phase pattern over the TP and better capture the features of the diurnal cycle of summer precipitation compared with TRMM 3B42(Zhang et al.,2015).

NCEP Final Analysis (FNL) data was used through dynamic downscaling as observed moisture to illustrate the transportation of water vapor in East Asia.

2.1.3 Assimilation data

The conventional data which is from the GDAS-prepared BUFR files (gdas1.tCCz.prepbufr.nr) is composed of a global set of surface and upper air reports operationally collected by the National Centers for Environmental Prediction (NCEP). It includes radiosondes, surface ship and buoy observations, surface observations over land, pibal winds and aircraft reports from the Global Telecommunications System (GTS), profiler and US radar derived winds, SSM/I oceanic winds and TCW retrievals, and satellite wind data from the National Environmental Satellite Data and Information Service (NESDIS). The reports can include pressure, geopotential height, temperature, dew point temperature, wind direction and speed. (National Centers for Environmental Prediction/National Weather Service/NOAA/U.S. Department of Commerce. 2008, updated

Atmos. Meas. Tech. Discuss., doi:10.5194/amt-2017-31, 2017
Manuscript under review for journal Atmos. Meas. Tech.
Discussion started: 27 February 2017

Atmospheric Measurement Techniques Discussions

147 daily. *NCEP ADP Global Upper Air and Surface Weather Observations (PREPBUFR format),*
148 *May 1997 - Continuing*.)

149 ATMS and CrIS satellite radiance data are also from the Global Data Assimilation System
150 (GDAS) which is in the BUFR format. All of this can be downloaded from
151 https://www.ncdc.noaa.gov/data-access/model-data/model-datasets/global-data-assimilation-
152 system-gdas.

153

154 *2.2 Models*

155 *2.2.1 WRF-ARW regional model*

156 NCAR's WRF-ARW regional model associated with the Gridpoint Statistical Interpolation
157 (GSI) data assimilation system was used in this study. WRF-ARW is a fully compressible
158 nonhydrostatic, primitive-equation, mesoscale meteorological model. As shown in Figure 1a, the
159 model domains are two-way nested with 12 km (580 × 422) and 4 km (817 × 574) horizontal
160 spacing. There are 51 vertical levels with a model top of 10 hPa. Figure 1 shows that D01 is set to
161 cover most of East Asia and the subdomain (D02) inside corresponds to the Tibetan Plateau, which
162 has a mountain–valley structure.

163 The physical parameterizations chosen for the forecast model in this study followed previous
164 studies of the area (He et al., 2012; Xu et al., 2012; Zhu et al., 2014). These included the WRF-
165 ARW Single-Moment 6-class (WSM-6) microphysics scheme, the Kain-Fritsh (KF) cumulus
166 parameterization, the Rapid Radiative Transfer Model (RRTMG) longwave and shortwave

Atmos. Meas. Tech. Discuss., doi:10.5194/amt-2017-31, 2017
Manuscript under review for journal Atmos. Meas. Tech.
Discussion started: 27 February 2017

Atmospheric Measurement Techniques Discussions

167 radiation, the Yonsei University scheme (YSU) and the Noah Land Surface Model for the planetary
168 boundary layer scheme.
169
170 *2.2.2 GSI system and Community Radiative Transfer Model*
171 In this study, we chose to use the GSI 3D-Var system, which is a data assimilation system that
172 was initially developed as the next-generation analysis system based on the operational Spectral
173 Statistical Interpolation (SSI) at NCEP (Derber and Wu, 1998). .
174 The development of fast radiative transfer models has allowed for the direct assimilation of
175 satellite infrared and microwave radiances in NWP systems (Saunders et al., 1999; Gauthier et al.,
176 2007; Zou et al., 2011). The Community Radiative Transfer Model (CRTM) developed by the
177 United States Joint Center for Satellite Data Assimilation (JCSDA) has been incorporated into the
178 NCEP GSI system to rapidly calculate satellite radiances (Han, 2006; Weng, 2009). In this study,
179 the ATMS and CrIS satellite radiance data can be read in GSI via CRTM 2.1.3. It is worth noticing
180 that the CrIS scans a 2200km swath width (+/- 50 degrees), with 30 Earth-scene views. Each field
181 consists of 9 fields of view, arrayed as 3x3 array of 14km diameter spots (nadir spatial resolution).
182 (https://jointmission.gsfc. nasa.gov/cris.html). The ATMS scans a 2300km swath width with 96
183 Earth-scene views. The 1-2 channel of the spatial resolution of ATMS at nadir is 75km; 3-6
184 channel is 32km; 17-22 channel is 16km (Dong et al., 2014).
185 *2.3 Radiance data quality control*

Atmos. Meas. Tech. Discuss., doi:10.5194/amt-2017-31, 2017
Manuscript under review for journal Atmos. Meas. Tech.
Discussion started: 27 February 2017

Atmospheric Measurement Techniques Discussions

As the quality of the observational data is easily affected by the observation instruments, station positions, or human factors, carrying out quality control before data application is necessary (Hubbard and You, 2005). Before data assimilation, a multiple-step quality control procedure was applied to the satellite radiance data in the GSI system and preprocessed by NOAA's Satellite and Information Service (NESDIS). Besides data thinning, it can be summarized to several quality control (QC) categories in GSI to either toss the questionable observations or inflate the low confidence observations. QC1: the observation-minus-model index based on liquid water path and brightness temperature is calculated to check the cloud affected profile; QC2: toss the channel of inaccurate emissivity/surface temperature estimate over sea; QC3: inflate observation error over high terrain; QC4: retrieved the profiles which meet criterion in QC1 and QC2. The observational number of ATMS data ranging from 53042 to 68618 in contrast to the number of CrIS data ranging from 2694048 to 3454542 are read in DA system. After the data had passed rigorous quality assessment and quality control processes, the results showed that about 23.2%-26.4%, and 1.3% and 1.6% of "good" observations related to ATMS and CrIS read data separately were retained after quality control (Fig. 2). This difference can be explained that CrIS has 1305 channel satellite radiance data, but the number of assimilated channels are significantly reduced (Table 2), the selection of redundant channel leads to some part of observation radiance data comes from the similar altitude and contains large amount of repeated information. Therefore, larger percentage of CrIS satellite radiance data than ATMS is tossed through QC steps. Figure 1(b) shows the distribution of the conventional data at 06:00 UTC on 1 July 2015, where observational data are

Atmos. Meas. Tech. Discuss., doi:10.5194/amt-2017-31, 2017
Manuscript under review for journal Atmos. Meas. Tech.
Discussion started: 27 February 2017

Atmospheric Measurement Techniques Discussions

206 rare in the TP. Figure 1c and 1d displays the distribution of satellite data after quality control,
207 where there is almost complete spatial coverage in East Asia including the TP.
208
209 **3. Method and experimental design**
210 *3.1 Method*
211 A basic two-by two contingency table (Table 1) was generated to calculate the Bias Score
212 (BIAS), Fraction skill Score (FSS), Equitable Threat Score (ETS), Probability of False Detection
213 (POFD), Probability of Detection (POD), and False Alarm ratio (FAR).
214 The BIAS, which measures the ratio of the frequency of forecast events to the frequency of
215 observed events, is defined as:
216 $$\mathrm{BIAS} = \frac{\text{Hits+False alarms}}{\text{Hits+Misses}} \quad (1)$$
217 The FSS introduced by Roberts and Lean (2008) is a neighborhood verification method. The FSS
218 is defined as:
219 $$\mathrm{FSS} = 1 - \frac{FBS}{FBS_{ref}} \quad (2)$$
220 Fractions Brier Score (FBS) is presented as
221 $$\mathrm{FBS} = \frac{1}{N}\sum_{i=1}^{N}[F_o - F_f]^2 \quad (3)$$
222 Where N is the number of all grid points in the domain. F_o and F_f are the observation and forecast
223 fractions of the sliding window at each grid point. The sliding window in this study is 100km (25
224 grid points). The reference Fractions Brier Score (FBS_{ref}) represent a largest possible FBS and is
225 given as：

Atmos. Meas. Tech. Discuss., doi:10.5194/amt-2017-31, 2017
Manuscript under review for journal Atmos. Meas. Tech.
Discussion started: 27 February 2017

Atmospheric Measurement Techniques Discussions

$$FBS_{ref} = \frac{1}{N}\left[\sum_{i=1}^{N} {F_o}^2 + \sum_{i=1}^{N} {F_f}^2\right] \quad (4)$$

The ETS computes the fraction of observed events that were correctly predicted:

$$\mathrm{ETS} = \frac{\mathrm{Hits}-R}{\mathrm{Hits+False\ alarms+Misses}-R} \quad (5)$$

where R is the random forecast coefficient, given by:

$$\mathrm{R} = \frac{(\mathrm{Hits+False\ alarms})(\mathrm{Hits+Misses})}{(\mathrm{Hits+False\ alarms+Misses+Correct\ rejections})} \quad (6)$$

The POFD measures discrimination:

$$\mathrm{POFD} = \frac{\mathrm{False\ alarms}}{\mathrm{False\ alarms+Correct\ rejections}} \quad (7)$$

Similar to the POFD, the POD shows the hits out of total observed events:

$$\mathrm{POD} = \frac{\mathrm{Hits}}{\mathrm{Hits+Misses}} \quad (8)$$

The FAR indicates the fraction of the predicted events that did not occur:

$$\mathrm{FAR} = \frac{\mathrm{False\ alarms}}{\mathrm{Hits+False\ alarms}} \quad (9)$$

To compare the model simulation data with the observation data, the 4-km model grid was interpolated to observation data with $0.1^{o}\times0.1^{o}$ degree grid based on linear interpolation method.

3.2 Experimental design

Four one-month-long experiments were conducted (Fig. 3). The CTRL experiment was carried out first with an initial time of 00:00 UTC and made 54 h forecasts. The data assimilation was applied on the D01 region of the output from CTRL at 06:00 UTC. The DA experiments made use of the assimilated D01 and the D02 from the CTRL at 06:00 UTC as the initial condition and made a 48 h forecast for each day. Three DA experiments were performed with a time window of 3 hours:

Atmos. Meas. Tech. Discuss., doi:10.5194/amt-2017-31, 2017
Manuscript under review for journal Atmos. Meas. Tech.
Discussion started: 27 February 2017

Atmospheric Measurement Techniques Discussions

246 (1) a conventional run (CONV) assimilating the conventional observation data only; (2) an ATMS
247 radiance run (ATMS) adding the ATMS satellite radiance data to the CONV; and (3) a CrIS
248 radiance run (CRIS) adding the CrIS satellite radiance data to the CONV.

249 The accumulated precipitation integrated from 06 to 30 h and 30 to 54 h are defined as the
250 first twenty-four-hour accumulated (F24H) precipitation and last twenty-four-hour accumulated
251 (L24H) precipitation, respectively.

252

253 **4. Results**

254 *4.1 Impact of DA on the spatial fields of precipitation forecast*

255 Figure 4 shows the spatial pattern of the monthly mean of 24-hour accumulated precipitation
256 in July 2015. Monthly mean precipitation exhibits a decreasing south-to-north gradient. The
257 predicted precipitation in the central and northern parts of the TP, Qaidam Basin (90°-99°E, 35°-
258 39°N), Tarim Basin (75°-90°E, 37°-42°N), and Junggar Basin (80°-90°E, 45°-48°N) was too small
259 to be measured (Fig. 4a, c). It was found that F24H precipitation ranged from 6.0 to 30.4 mm,
260 while the L24H forecasts ranged from 6.0 to 29.5 mm per month. The rain shadow along the
261 Himalayas (73°-95°E, 27°-35°N) was found in the spatial distribution of precipitation. The CTRL
262 (Fig. 4b, d) mostly simulated the monthly mean rainbelt distributed along the southern and
263 southwestern margin of the plateau, between the Himalayas in the west and the Hengduan
264 Mountains (95°-103°E, 24°-32°N) in the east. The difference between the model simulations and
265 observations (Fig. 5) indicated that the CTRL simulation tends to overestimate precipitation,

Atmos. Meas. Tech. Discuss., doi:10.5194/amt-2017-31, 2017
Manuscript under review for journal Atmos. Meas. Tech.
Discussion started: 27 February 2017

especially in the southern and southwestern margin along the rainbelt where the altitude changes from 500 to 3000 m. The results suggested that the WRF-ARW model has limitations in simulating the precipitation in mountainous areas, which is similar to the conclusion of previous studies (He et al., 2012; Xu et al., 2012). Furthermore, we found that the precipitation is overestimated (colored red) in the upwind of the mountains along the southwestern margin. In contrast, the precipitation is underestimated in the south of the rainbelt, leading to a north–south dipole structure. This pattern results in a northward migration of the rainbelt in the simulations. The three DA experiments indicated that the assimilation of satellite radiance data can not calibrate the rain shadow effect and all experiments showed consistently gross overestimation patterns, varying from 8 to 10 mm about the monthly mean precipitation. The overall bias statistic in D02 is 0.97 mm (0.86 mm), 0.52 mm (0.70 mm), 1.08 mm (0.97 mm), and 0.98 mm (0.76 mm) CTRL, CONV, ATMS and CRIS respectively. This may be attributed to the physical package of WRF-ARW having an inadequate description of snow cover over the plateau surface making the error of margin more prominent (Marteau et al. 2015).

Figure 6 shows the spatial patterns according to the contingency table (Table 1) and the scatter plots, in which monthly mean 24 h rainfall over the 6 mm threshold is defined as an “event”. Rainfall events occur over most of the TP area, including the northern Gangetic Plain (80°-90°E, 24°-28°N) where the elevation is lower than 3000 m, and can be well predicted with ~8–10% hits (A) and ~76–79% correct rejections (D) in the majority of the region. The false alarms (B) were spread mainly in the east of the TP, where the Bayan Har (95°E, 35°N) and Hengduan mountains

Atmos. Meas. Tech. Discuss., doi:10.5194/amt-2017-31, 2017
Manuscript under review for journal Atmos. Meas. Tech.
Discussion started: 27 February 2017

Atmospheric Measurement Techniques Discussions

286 are located, accounting for ~7–10%, while the misses (C) were distributed in the western plain
287 exterior of the TP and accounted for ~5–6%. It's also evident to see the dipole pattern in the
288 distribution of the hits and misses similar to the Figure 5. Among the four linear regression lines
289 (bold grey lines), ATMS looks a little better than the other three experiments but has more extreme-
290 precipitation event forecasts than the others, followed by the CTRL and CRIS, while CONV has
291 the lowest simulation precision. This implies that the rain shadow mainly influences prediction of
292 the quantity of precipitation, but rainfall events are still well predicted. Furthermore, the
293 comparisons indicated that the WRF-ARW model has promising potential, as the false alarms were
294 primarily located in the east of the TP in contrast to the misses in the west.

295 Figure 7 shows the monthly and domain average validation statistics in the TP. The differences
296 between the four experiments for the F24H forecasts are larger than for the L24H forecasts. The
297 ETS, FSS, and POD values all decline as the threshold increases; a higher value for these three
298 skill scores indicates a better performance of the experiments. ATMS showed the highest FSS (Fig.
299 7b), ETS (Fig. 7c) and POD (Fig. 7d). CONV performed similar to the CTRL in ETS and FSS,
300 and CRIS performed the worst. However, according to the BIAS, CONV is mostly approximately
301 1, which indicates the best overall relative frequencies compared with the other experiments.
302 Through the 1–5 mm threshold, CRIS performs the largest overforecast (BIAS > 1), but it evolves
303 to have a better performance than ATMS and CTRL through the 5–10 mm threshold. FAR and
304 POFD results indicate that CONV performs best (0 is perfect), followed by ATMS and then CTRL
305 and CRIS. However, POD results manifest that ATMS performs best (1 is perfect) and CONV is

Atmos. Meas. Tech. Discuss., doi:10.5194/amt-2017-31, 2017
Manuscript under review for journal Atmos. Meas. Tech.
Discussion started: 27 February 2017

306 worst. The different methods of forecast verification may depend on the purpose of the verification,
307 and the results we evaluated by different methods can explain the different question we want to
308 answer. Overall, the results reflect that DA has a positive effect on reproducing the monthly mean
309 precipitation in the TP compared with the CTRL to varying degrees.
310
311 *4.2 Impact of DA on the temporal distribution of precipitation forecast*
312 Another measure of performance is to examine how the daily precipitation is temporally
313 distributed (Fig. 8). It can be seen in the time series that there are four observed heavy rainfall
314 events(3.0 mm/day) during the periods of 3–6, 8-10，13–16 and 22–25 July (Fig. 8a). In general,
315 the 24 h amount of precipitation is overestimated in all three DA experiments by 20%, 40%, and
316 37% for CONV, ATMS, and CRIS, respectively. In contrast, of the 4 heavy rainfall periods, 3
317 events including 3–6, 13–16 and 22–25 July are underestimated. The L24H forecasts showed a
318 similar pattern, except that there were much smaller differences between the three DA experiments
319 compared with the F24H forecasts. The F24H forecasts appear the one-day time lag effect
320 compared with L24H. Because the F24H forecasts calculate the cumulative precipitation of the
321 first 6-30 hour while the L24H forecasts represent the 30-54 hour cumulative precipitation
322 forecasts. When all the overestimation events are considered, the CONV experiment captured the
323 accumulated amount of precipitation much more accurately than the other DA experiments and the
324 ATMS performed the worst. As mentioned above, the 24 h precipitation maximums surpassing 20

Atmos. Meas. Tech. Discuss., doi:10.5194/amt-2017-31, 2017
Manuscript under review for journal Atmos. Meas. Tech.
Discussion started: 27 February 2017

Atmospheric Measurement Techniques Discussions

mm are spread in the main precipitation region, showing that the prominent geographical dependence of rainfall coincides with the threshold of heavy rainfall defined for TP areas.

Although previous studies and our results show an obvious trend of overestimating rainfall in the TP, there appears to be underestimated during heavy rainfall events (Fig. 8). To determine the forecast capabilities of the model in the heavy rainfall periods, we focused on one heavy rainfall period of 3-6 July.

Figure 9 shows the rainfall intensities (bars) calculated for every 3 h amount of precipitation. The cumulative precipitation (curves) is defined as the precipitation accumulated for each 3 h starting at 06:00 UTC during 3–6 July. From the perspective of observations, this rainfall event can be divided into three periods, of which the 3 July is ahead of the heavy rainfall with less than 0.45 mm per 3 h, followed by the rainfall around 03:00 UTC on 4 July to 03:00 UTC on 5 July, with the first peak at 21:00 UTC on 4 July of more than 0.65 mm per 3 h. The third phase started at 03:00 UTC on 5 July and ended at 00:00 UTC on 6 July with a second rainfall pulse around 21:00 UTC on 5 July exceeding 0.60 mm per 3 h and then weakening. It is evident that this rainfall event had a significant diurnal harmonic and the maximum precipitation always occurred at 18:00–21:00 UTC (00:00–03:00 LST). This diurnal variation was remarkable, especially when the heavy rainfall occurred, which was equivalent to evening local solar time (LST). However, the simulated maximum always occurred at 06:00–09:00 UTC (12:00–15:00 LST), earlier than the observations, and can probably be attributed to the limit of complicated topography. In this case, simulated rainfall intensity was much lower than the observations during 09:00 UTC on 4 July to 00:00 UTC

Atmos. Meas. Tech. Discuss., doi:10.5194/amt-2017-31, 2017
Manuscript under review for journal Atmos. Meas. Tech.
Discussion started: 27 February 2017

Atmospheric Measurement Techniques Discussions

345 on 5 July and 12:00 UTC on 5 July to 21:00 UTC on 5 July when the rainfall occurred. That is, the
346 model can not promptly quantitatively predict the sudden occurrence of this event. Moreover, the
347 cumulative curves of the model show an overestimation on 3 and 5 July compared with
348 observations; in particular, the cumulative curves of the CTRL are far away from the measured
349 values due to an inaccurate initial field. It can be concluded that the DA experimentsdata are closer
350 to the observations during the heavy rainfall period compared with the CTRL experiment.
351
352 *4.3 Impact of DA on circulation and water vapor supply*
353 According to the above-mentioned analysis, it is evident that DA improves forecasts during
354 the heavy rainfall period, but the results are not universal when different data sets are injected. As
355 is well known, adequate water vapor transport is one of the preconditions for precipitation
356 formation. In this section, we discuss the water vapor supply in the 3–6 July case study, with the
357 aim of determining the reason for the different influences exerted by different experimental
358 schemes. Figure 10 shows the F24H forecasts of precipitation quantity (shadings) and water vapor
359 flux (vectors) during 3–6 July. According to observations, warm and humid water vapor is
360 transferred from the Bay of Bengal eastward by the southwest monsoon. The TP blocks the
361 westward transport of humid and warm air, and this rainfall event start developing in the southeast
362 of the TP on 3 July and then the rainbelt runs southeast to southwest and develops along the
363 Himalayas on 4–5 July. Comparing the observations (Fig. 10a–c) with model results (Fig. 10d–f),
364 the simulated precipitation is considerably larger than the observed on 3 July before the heavy

Atmos. Meas. Tech. Discuss., doi:10.5194/amt-2017-31, 2017
Manuscript under review for journal Atmos. Meas. Tech.
Discussion started: 27 February 2017

365 rainfall occurs, but as time goes on this condition reverses. For the difference value distribution
366 (Fig. 10g–i) of the CTRL minus observations, the main water vapor flux divergence differences
367 (shadings) are negative in the rainy region on 3 July, which indicates that the water vapor
368 convergence is stronger than observed, inducing the overestimation. However, when the rainfall
369 event occurs on 4–5 July, this condition is opposite. The water vapor differences (vectors) also
370 suggest that the observed water vapor conveyance from the southeastern of the TP is larger than
371 the model simulation, which induces inaccuracies in the forecast of the heavy rain. Therefore,
372 analysis of moisture is useful for improving the heavy rainfall forecasting skill.

373 To further discuss the effect of DA on this rainfall event, the differences between the simulated
374 F24H precipitation and the observed distribution and the ETS skill scores (Fig. 11) were considered.
375 From the spatial distribution, all the experiments (Fig. 11a, d, g, j) overestimated the precipitation
376 quantity, especially the CTRL, before the heavy rainfall and the FSS skill scores all ranged from
377 0.46 to 0.49 with little differences (left in Fig. 11m). When the heavy rainfall event occurred on 4
378 July, the observed rainbelt moved southwest (Fig. 11b, e, h, k), while the simulated rainbelt was
379 motionless, leading to an underestimation in the southwest. The FSS scores for ATMS, CONV and
380 CTRL ranged from 0.42 to 0.48 (middle in Fig. 11m), but CRIS only scored 0.36. As the water
381 vapor conveyance directly contributes to the westward movement of the rainbelt and the intensity
382 of this precipitation event on 5 July, the precipitation experiments all underestimated the amount
383 of precipitation, and CRIS performed particularly badly (Fig. 10c, f, i, l). However, ATMS had a
384 substantially high FSS scores (0.47) (right in Fig. 11m), followed by CRIS(0.45) and CONV(0.43)

Atmos. Meas. Tech. Discuss., doi:10.5194/amt-2017-31, 2017
Manuscript under review for journal Atmos. Meas. Tech.
Discussion started: 27 February 2017

while CTRL only scored 0.35. This phenomenon indicates that DA can indeed improve the heavy rainfall forecast. From the above analysis of Figure 9 and 10, it is clear that before the heavy rainfall, DA can improve the simulation of precipitation spatially. As time passes and the heavy rainfall develops, DA, especially the ATMS assimilation, can enhance model prediction abilities both spatially and temporally in comparison with the CTRL experiment.

5. Summary and discussion

In this study, we used diagnostic methods to analyze the impact of DA on the monthly precipitation distribution over the TP and then focused on one heavy rainfall case study that occurred from 3 to 6 July 2015. The DA and NWP were performed for July 2015 to make the weather forecasts. The spatial distribution of monthly mean precipitation showed an evident rain shadow effect along the Himalayas and that the precipitation decreased northward in the TP. However, the simulated precipitation belt was shifted northward compared with the observed rainbelt and showed an orographic bias described as an overestimation in the upwind of the mountains and an underestimation in the south of the rainbelt. Assimilation of satellite radiance also can not calibrate the rain shadow effect and all experiments showed consistently gross overestimation patterns. Furthermore, it seems that the rain shadow mainly influences prediction of the quantity of precipitation, but the main rainfall pattern can be well predicted. Comparisons indicate that the WRF-ARW model has promising potential, in that the false alarms are primarily predicted in the east of the TP in contrast to the misses in the west. The DA validation statistics

405 also suggest that DA has a positive effect on monthly mean precipitation prediction in the TP
406 compared with the CTRL to varying degrees. For the time series of monthly precipitation, F24H
407 and L24H precipitation chiefly overestimate the amount of precipitation, which is in agreement
408 with previous studies, , but the amount of 24 h precipitation in the three heavy rainfall periods of
409 3–6, 13–16, and 22–25July is underestimated.

410 To further study the underestimations in the heavy rainfall events and the performance of the
411 WRF-ARW model and GSI DA impact, we selected a case study from 3 to 6 July. It is evident that
412 this rainfall event had a significant diurnal harmonic and the maximum precipitation always
413 occurred at 18:00–21:00 UTC (00:00–03:00 LST). This diurnal variation was remarkable,
414 especially when the heavy rainfall occurred. Although the model can not promptly quantitatively
415 predict the sudden occurrence of this rainfall event, the DA, especially the ATMS simulation are
416 closer to the observations for the heavy rainfall event compared with CTRL experiments. Overall,
417 before the heavy rainfall, DA improved the precipitation prediction spatially. As time passed and
418 the rainbelt moved and rainfall developed, DA enhanced the model prediction abilities both
419 spatially and temporally. It should be mentioned that the high altitude and complex topography of
420 the TP and its blocking effect on moisture transfer coming from Indian Ocean by the southwest
421 monsoon obviously influences the rainfall forecast. As precipitation biases indicate some extent of
422 spatial coherence and temporal recurrence, it is possible to provide an adapted correction method
423 to enhance the model precipitation prediction capabilities.

Atmos. Meas. Tech. Discuss., doi:10.5194/amt-2017-31, 2017
Manuscript under review for journal Atmos. Meas. Tech.
Discussion started: 27 February 2017

424 It is conspicuous that the ATMS showed better performance than CTRL, CONV, and CRIS in
425 the case study. Past studies have indicated that the effect of assimilation of both observations and
426 satellite products is better than assimilation of satellite data only, which may account for the ATMS
427 performing better than CONV. ATMS also performed better than CRIS. As clouds are opaque in
428 the infrared wave band of the spectrum and largely transparent in the microwave band, microwave
429 instruments are thought to perform better than infrared instruments on cloudy and rainy days,
430 which may explain the better performance of ATMS compared with CRIS.

431 In this study, we investigated the monthly precipitation distribution and a selected heavy
432 rainfall case in the TP using the WRF-ARW mesoscale model and the GSI data assimilation system.
433 Moisture and dynamic conditions were analyzed in the case study; however, thermal conditions
434 are also one of the direct factors leading to rainfall that need to be investigated in the future.

435 Furthermore, although the CrIS were assimilated large amount of satellite radiance pixels, the
436 general DA effect is relatively worse compared with the other three experiments. CrIS has 1305
437 spectral channels, some of which are redundant as they include many satellite radiance
438 observations from similar altitudes and contain much repeated information, which may lead to the
439 poor DA impact. It should take the priority to select physical sensitivity and the high vertical
440 resolution channels. On the other hand, the high altitude and complicated dynamic, thermal
441 conditions increase the difficulty of selecting channels. Therefore, only by carrying out further
442 research on bias correction, quality control, and channel selection can satellite radiance data play
443 an efficient role in TP weather forecasting.

Atmos. Meas. Tech. Discuss., doi:10.5194/amt-2017-31, 2017
Manuscript under review for journal Atmos. Meas. Tech.
Discussion started: 27 February 2017

Atmospheric Measurement Techniques Discussions

444 In addition, model resolution and parameterized scheme selection are also key factors
445 affecting forecast quality. In this study, the parameterized schemes we chose have been applied in
446 previous studies of the TP. It would be worthwhile to make a comparative analysis of different
447 parameterized schemes with higher model resolution in the future. Furthermore, it should be noted
448 that due to the heavy calculation burden, this study made use of 3D-Var as the assimilation method.
449 Other advanced assimilation techniques, such as 4D-Var, Hybrid, and EnKF, also need to be tested.
450

451 ***Acknowledgements***

452 The WRF-ARW model was obtained from NCAR, the GSI data assimilation system was obtained
453 from JCSDA, and the satellite datasets were provided by NOAA/NESDIS/STAR. The authors are
454 very grateful to these agencies for the model and providing data. This work was jointly supported
455 by the Special Fund for Public Welfare of China Meteorological Administration
456 (GYHY201406024) and the National Natural Science Foundation of China (91437104, 41330425,
457 41130960). The corresponding author was supported by the Guangdong Ocean University
458 Research Funding of Air–Sea Interaction and Data Assimilation (300702/E16188). The first author
459 was a visiting scholar at GMU/AOES during this study and acknowledges helpful discussions
460 with fellow members of GMU/AOES.
461
462

Atmos. Meas. Tech. Discuss., doi:10.5194/amt-2017-31, 2017
Manuscript under review for journal Atmos. Meas. Tech.
Discussion started: 27 February 2017

Atmospheric Measurement Techniques Discussions

463 **References**

464 Bormann, N., A. Fouilloux, and W. Bell: Evaluation and assimilation of ATMS data in the ECMWF
465 system, *Journal of Geophysical Research: Atmospheres*, *118*(23), 2013

466 Chambon, P., S. Q. Zhang, A. Y. Hou, M. Zupanski, and S. Cheung: Assessing the impact of pre-
467 GPM microwave precipitation observations in the Goddard WRF ensemble data assimilation
468 system, *Quarterly Journal of the Royal Meteorological Society*, *140*(681), 1219-1235, 2014

469 Chen, Y., L. Ji, and R. Shen: The numerical experiments on dynamic forcing by the Tibetan Plateau
470 for various zonal flows, *Advances in Atmospheric Sciences*, *2*(2), 189-199, 1985

471 Derber, J. C., and W. S. Wu: The use of TOVS cloud-cleared radiances in the NCEP SSI analysis
472 system, *Monthly Weather Review*, *126*(8), 2287-2299, 1998

473 Dong, P., Liu, J., Liu, G., & Huang, J.: Study on the assimilation of ATMS satellite data and
474 comparison with AMSUA/MHS, *Journal of Tropical Meteorology*, 30(4), 623-632, 2014

475 Eyre, J. R.: *A bias correction scheme for simulated TOVS brightness temperatures*, European
476 Centre for Medium-Range Weather Forecasts, 1992

477 Gao, Y., J. Xu, and D. Chen: Evaluation of WRF Mesoscale Climate Simulations over the Tibetan
478 Plateau during 1979–2011, Journal of Climate, 28(7), 2823-2841, 2015

479 Gauthier, P., M. Tanguay, S. Laroche, S. Pellerin, and J. Morneau: Extension of 3DVAR to 4DVAR:
480 Implementation of 4DVAR at the Meteorological Service of Canada, Mon. Wea. Rev., 135,
481 2339–2354, 2007

482 Guo, J., Zhai, P., Wu, L., Cribb, M., Li, Z., Ma, Z., & Zhang, J.: Diurnal variation and the
483 influential factors of precipitation from surface and satellite measurements in

Tibet, *International Journal of Climatology*, *34*(9), 2940-2956, 2014

Han, Y., P. Delst, Q. Liu, F. Weng, B. Yan, R. Treadon, and J. Derber: JCSDA Community Radiative Transfer Model-Version 1 (CRTM-V1), *NOAA Tec,* (122), 40, 2006

He, Y., K. Yang, T. Yao, and J. He: Numerical Simulation of a Heavy Precipitation in Qinghai-Xizang Plateau Based on WRF Model, *Plateau Meteorology (in Chinese)*, 31(5), 1185-1186, 2012

Hubbard, K. G., and J. You: Sensitivity analysis of quality assurance using the spatial regression approach-A case study of the maximum/minimum air temperature, *Journal of Atmospheric and Oceanic Technology*, *22*(10), 1520-1530, 2005

Kazumori, M.: Satellite radiance assimilation in the JMA operational mesoscale 4DVAR system, *Monthly Weather Review*, *142*(3), 1361-1381, 2014.

Liu, Q. and F. Weng: Detecting the warm core of a hurricane from the Special Sensor Microwave Imager Sounder, Geophys. Res. Lett., 33, 2006

Liu, Z., C. S. Schwartz, C. Snyder, and S. Y. Ha: Impact of assimilating AMSU-A radiances on forecasts of 2008 Atlantic tropical cyclones initialized with a limited-area ensemble Kalman filter, *Monthly Weather Review*, *140*(12), 4017-4034, 2012

Liu, J., M. Bray, and D. Han: A study on WRF radar data assimilation for hydrological rainfall prediction, *Hydrology and Earth System Sciences*, *17*(8), 3095-3110, 2013

502 Marteau, R., Y. Richard, B. Pohl, C. C. Smith, and T. Castel: High-resolution rainfall variability
503 simulated by the WRF RCM: application to eastern France, *Climate Dynamics*, *44*(3-4),
504 1093-1107, 2015
505 Massacand, A. C., H. Wernli, and H. C. Davies: Heavy precipitation on the Alpine southside: An
506 upper-level precursor, *Geophysical Research Letters*, *25*(9), 1435-1438, 1998
507 Maussion, F., D. Scherer, R. Finkelnburg, and J. Richters: WRF simulation of a Precipitation event
508 over the Tibetan Plateau, China-an assessment using remote sensing and ground observations,
509 2011
510 Newman, K. M., C. S. Schwartz, Z. Liu, H. Shao, and X.-Y. Huang: Evaluating Forecast Impact
511 of Assimilating Microwave Humidity Sounder (MHS) Radiances with a Regional Ensemble
512 Kalman Filter Data Assimilation System, *Weather and Forecasting*, *30*(4), 964-983, 2015
513 Pan, Y., Y. Shen, Q.-Q. Yu, and P. Zhao: Merged analyses of gauge-satellite hourly precipitation
514 over China based on OI technique (in Chinese with English abstract), Acta Meteor. Sin, 70,
515 1381-1389, 2012
516 Roberts, N. M., and H. W. Lean: Scale-selective verification of rainfall accumulations from high-
517 resolution forecasts of convective events, Mon. Wea. Rev., 136, 78–97, 2008
518 Saunders, R., M. Matricardi, and P. Brunel: An improved fast radiative transfer model for
519 assimilation of satellite radiance observations, *Quarterly Journal of the Royal Meteorological*
520 *Society*, *125*(556), 1407-1425, 1999
521 Schwartz, C. S., Z. Liu, Y. Chen, X. Y. Huang: Impact of assimilating microwave radiances with a

limited-area ensemble data assimilation system on forecasts of Typhoon Morakot, *Weather and Forecasting*, *27*(2), 424-437, 2012.

Shen, Y., P. Zhao, Y. Pan, and J. Yu: A high spatiotemporal gauge-satellite merged precipitation analysis over China, *Journal of Geophysical Research: Atmospheres*, *119*(6), 3063-3075, 2014.

Wang, C. H., S. W. Zhou, X. P. Tang, and P. Wu: Temporal and spatial distribution of heavy precipitation over Tibetan Plateau in recent 48 years, *Scientia Geographica Sinica*, *31*(4), 470-477, 2011.

Wei, Z., R. H. Huang, W. J. Dong: Interannual and interdecadal variations of air temperature and precipitation over the Tibetan Plateau, *Chinese Journal of Atmospheric Sciences*, 27(2), 157-170, 2003

Weng, F.: Advances in radiative transfer modeling in support of satellite data assimilation. *Hyperspectral Imaging and Sensing of the Environment* (p. HWD1), Optical Society of America, 2009

Xie, P., and A. Y. Xiong: A conceptual model for constructing high-resolution gauge-satellite merged precipitation analyses, *Journal of Geophysical Research: Atmospheres*, 116(D21) , 2011

Xu, J., S. Rugg, L. Byerle, and Z. Liu: Weather forecasts by the WRF-ARW model with the GSI data assimilation system in the complex terrain areas of southwest Asia, *Weather and Forecasting*, *24*(4), 987-1008, 2009

542 Xu, J., B. Zhang, M. Wang, and H. Wang: Diurnal variation of summer precipitation over the
543 Tibetan Plateau: a cloud-resolving simulation, *Annales Geophysicae,* 30(11), 1575-1586,
544 2012
545 Xu, J. and A. Powell: Dynamical downscaling precipitation over the Southwest Asian: impacts of
546 radiance data assimilation on the hindcasts of the WRF-ARW model, Atmos. Res., 111, 90–
547 103, 2012
548 Ye, D. Z., and Y. X. Gao: Tibetan Plateau Meteorology. *Science, Beijing*, 89-101, 1979
549 Zapotocny, T. H., J. A. Jung, J. F. Le Marshall, and R. E. Treadon: A two-season impact study of
550 four satellite data types and rawinsonde data in the NCEP Global Data Assimilation
551 System, *Weather and Forecasting*, *23*(1), 80-100, 2008
552 Zhang, X., X, B., & X, K.: Observed diurnal cycle of summer precipitation over South Asia and
553 East Asia based on CMORPH and TRMM satellite data, *Atmospheric and Oceanic Science*
554 *Letters*, *8*(4), 201-207, 2015
555 Zhao, X. Y., Y. R. Wang, Q. Zhang, and L. Luo: Climatic characteristics of heavy precipitation
556 events during summer half year over the Eastern Tibetan Plateau in recent 50 years, *Arid Land*
557 *Geography*, *4*, 004, 2015.
558 Zhu, F., G. Xu, and L. Li: An assessment of the impact on precipitation prediction in the middle
559 and lower reaches of the Yangtze River made by assimilating GPSPW data in the Tibetan
560 Plateau, *Chinese Journal of Atmospheric Sciences (in Chinese)*, 38 (1): 171–189, 2014
561 Zhu, Y., J. Derber, A. Collard, D. Dee, R. Treadon, G. Gayno, and J. A. Jung: Enhanced radiance
562 bias correction in the National Centers for Environmental Prediction's Gridpoint Statistical

Atmos. Meas. Tech. Discuss., doi:10.5194/amt-2017-31, 2017
Manuscript under review for journal Atmos. Meas. Tech.
Discussion started: 27 February 2017

563 Interpolation Data Assimilation System., Meteorol. Soc, 2013

564 Zou, X., Z. Qin, and F. Weng: Improved coastal precipitation forecasts with direct assimilation of

565 GOES-11/12 imager radiances, *Monthly Weather Review*, *139*(12), 3711-3729, 2011

566 Zou, X., Z. Qin, and F. Weng: Improved quantitative precipitation forecasts by MHS radiance data

567 assimilation with a newly added cloud detection algorithm, *Monthly Weather Review*, *141*(9),

568 3203-3221, 2013.

569

Atmos. Meas. Tech. Discuss., doi:10.5194/amt-2017-31, 2017
Manuscript under review for journal Atmos. Meas. Tech.
Discussion started: 27 February 2017

Atmospheric Measurement Techniques Discussions

570 **Table 1.** Contingency table.

Forecast	Observed	
	Yes	No
Yes	Hits	False alarms
No	Misses	Correct rejections

571

572

573 **Table 2.** The channels for ATMS and CrIS data have been selected in the data assimilation

Sensor	Channels
ATMS	1-14, 16-22
CrIS	37, 49, 51, 53, 59, 61, 63, 65, 67, 69, 71, 73, 75, 77, 79, 80, 81, 83, 85, 87, 89, 93, 95, 96, 99, 101, 102, 104, 106, 107, 116, 120,123, 124,,125, 126, 130, 132, 133, 136, 137, 138, 142,143, 144, 145, 147, 148, 150, 151, 153, 154, 155, 157-168, 170, 171, 173, 175, 198, 211, 224, 279, 342, 392, 404, 427, 464, 482, 501, 529

574

575

576

577

578

579

580

581

Atmos. Meas. Tech. Discuss., doi:10.5194/amt-2017-31, 2017
Manuscript under review for journal Atmos. Meas. Tech.
Discussion started: 27 February 2017

Atmospheric Measurement Techniques Discussions

582 **Figure captions**

583 **Figure 1.** (a) Simulation domains. (b)–(d) Distribution of (b) conventional data observations, (c)
584 scan coverage of ATMS data after data assimilation, and (d) scan coverage of CrIS data
585 after data assimilation at 06:00 UTC on 1 July 2015.

586 **Figure 2.** Total number of radiance observations kept and used in the forecast experiments as a
587 function of date for the (a) ATMS and (b) CrIS data

588 **Figure 3.** Experiments design, CTRL: control experiment without data assimilation; CONV: data
589 assimilation with conventional data only; ATMS: data assimilation with conventional
590 +ATMS data; CRIS: data assimilation with conventional + CrIS data

591 **Figure 4.** Spatial pattern of the monthly mean precipitation (unit: mm) in July 2015. (a),(b)
592 F24Hforecast and (c),(d) L24Hforecast. Contours are altitude (unit: m).

593 **Figure 5.** Difference value distribution of monthly mean precipitation (unit: mm) during July for
594 data assimilation minus observation experiments. (a), (e) CTRL minus OBS; (b), (f)
595 CONV minus OBS; (c), (g) ATMS minus OBS for (a)–(d) F24Hforecast and (e)–(h)
596 L24Hforecast. Contours are altitude (unit: m).

597 **Figure 6.** Spatial patterns of (a)–(d) the contingency table and (e)–(h) the scatter plots (monthly
598 mean 24 h rainfall over 6 mm threshold is defined as an “event”). The solid grey line
599 indicate the regression line of A. Contours are altitude (unit: m).

600 **Figure 7.** Monthly and domain average validation statistics. (a)–(f) F24Hforecast and (g)–(l)
601 L24Hforecast.

Atmos. Meas. Tech. Discuss., doi:10.5194/amt-2017-31, 2017
Manuscript under review for journal Atmos. Meas. Tech.
Discussion started: 27 February 2017

Atmospheric Measurement Techniques Discussions

602 **Figure 8.** Daily precipitation distribution (unit: mm).

603 **Figure 9.** Rainfall intensities (bars) calculated for every 3 h amount of precipitation. The
604 cumulative precipitation (curves) is defined as the precipitation accumulated for each 3
605 h starting at 06:00 UTC during 3–6 July. The unit is mm.

606 **Figure 10.** (a)–(f) 24 h forecasts of precipitation quantity (shadings) and water vapor flux (vectors)
607 during 3–6 July for (a)–(c) OBS and (d)–(f) CTRL. (g)–(i) Differences in water vapor
608 flux (vectors) and water vapor divergence (shadings) between CTRL and OBS. The unit
609 of precipitation quantity is mm. The units for water vapor flux and divergence is kg/(m*s)
610 and kg/(m^2*s), respectively.

611 **Figure 11.** Differences between (a)–(l) the simulated F24H precipitation and the observed
612 distribution and (m) the FSS skill scores with 8 mm threshold during 3–6 July. The unit
613 of differences is mm.

614

Atmos. Meas. Tech. Discuss., doi:10.5194/amt-2017-31, 2017
Manuscript under review for journal Atmos. Meas. Tech.
Discussion started: 27 February 2017

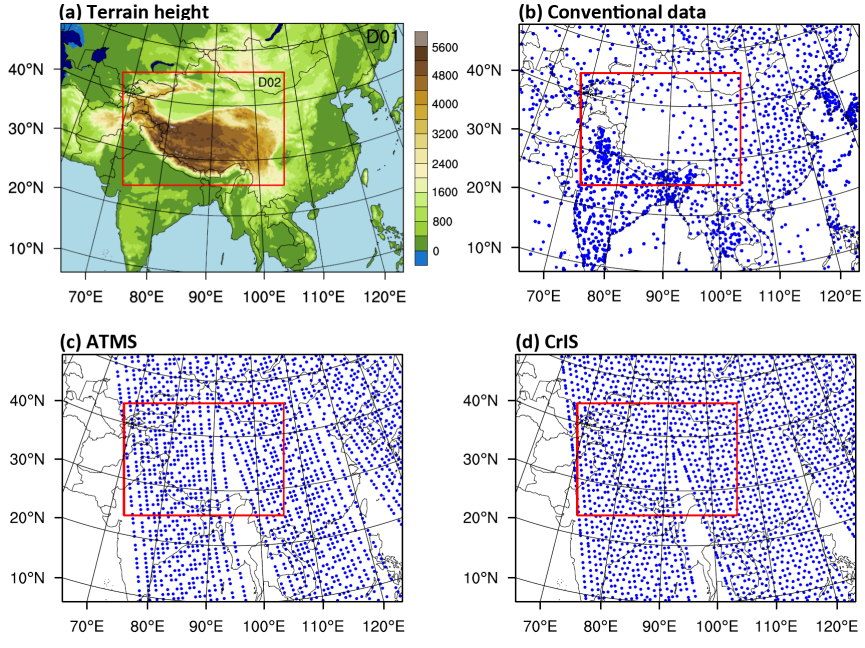

615

616 **Figure 1.** (a) Simulation domains. (b)–(d) Distribution of (b) conventional data observations, (c) scan coverage of ATMS data after data

617 assimilation, and (d) scan coverage of CrIS data after data assimilation at 06:00 UTC on 1 July 2015.

Atmos. Meas. Tech. Discuss., doi:10.5194/amt-2017-31, 2017
Manuscript under review for journal Atmos. Meas. Tech.
Discussion started: 27 February 2017

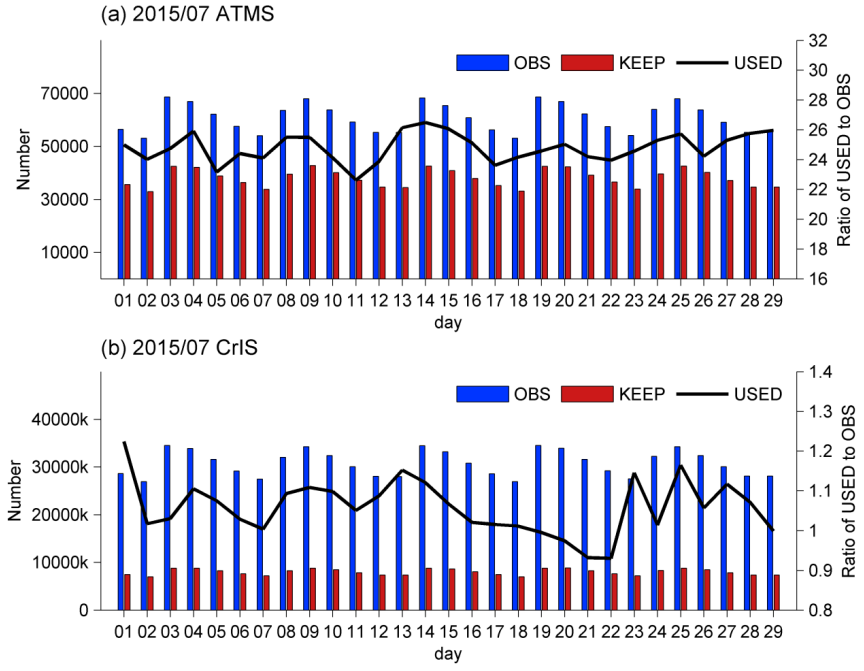

618

619 **Figure 2.** Total number of radiance observations kept and used in the forecast experiments as a function of date for the (a) ATMS and (b) CrIS

620 data.

Atmos. Meas. Tech. Discuss., doi:10.5194/amt-2017-31, 2017
Manuscript under review for journal Atmos. Meas. Tech.
Discussion started: 27 February 2017

Atmospheric Measurement Techniques Discussions

621

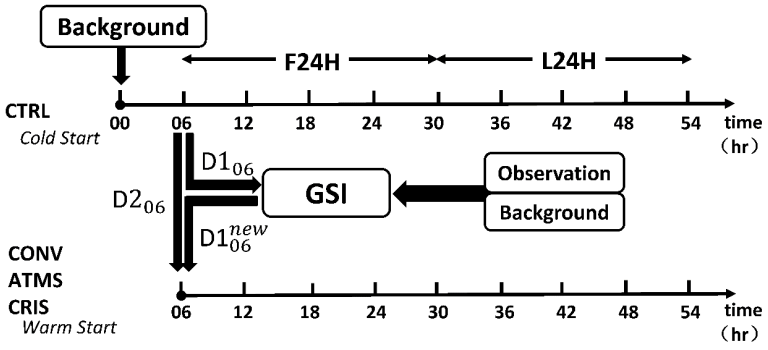

EXP	Description	Initial time
CTRL	No assimilation	00:00 UTC from 1 Jul to 31 Jul
CONV	Conventional data only	06:00 UTC from 1 Jul to 31 Jul
ATMS	Conventional + ATMS data	06:00 UTC from 1 Jul to 31 Jul
CRIS	Conventional + CrIS data	06:00 UTC from 1 Jul to 31 Jul

622

623 **Figure 3.** Experiments design, CTRL: control experiment without data assimilation; CONV: data assimilation with conventional data only; ATMS:

624 data assimilation with conventional +ATMS data; CRIS: data assimilation with conventional + CrIS data

Atmos. Meas. Tech. Discuss., doi:10.5194/amt-2017-31, 2017
Manuscript under review for journal Atmos. Meas. Tech.
Discussion started: 27 February 2017

Atmospheric Measurement Techniques Discussions

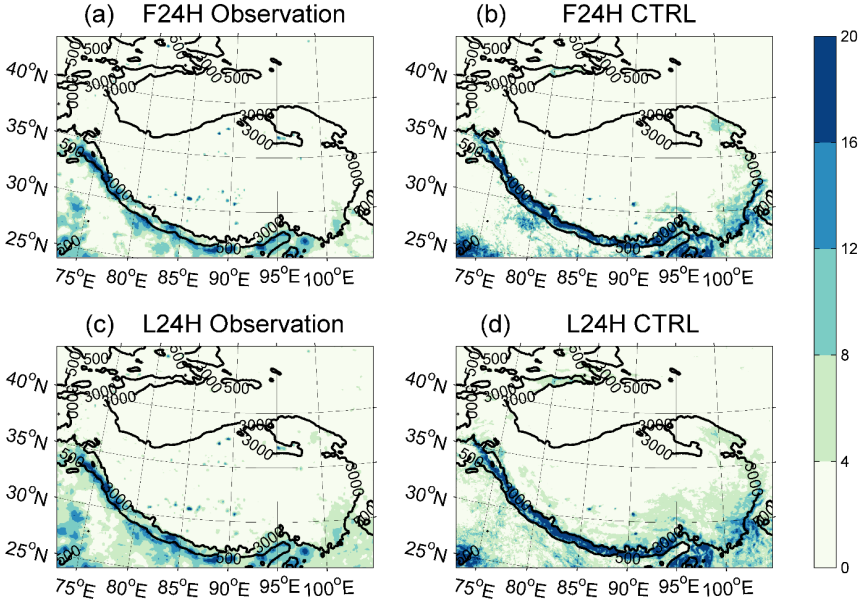

625

626 **Figure 4.** Spatial pattern of the monthly mean precipitation (unit: mm) in July 2015. (a), (b) F24H forecast and (c), (d) L24Hforecast. Contours

627 are altitude (unit: m).

Atmos. Meas. Tech. Discuss., doi:10.5194/amt-2017-31, 2017
Manuscript under review for journal Atmos. Meas. Tech.
Discussion started: 27 February 2017

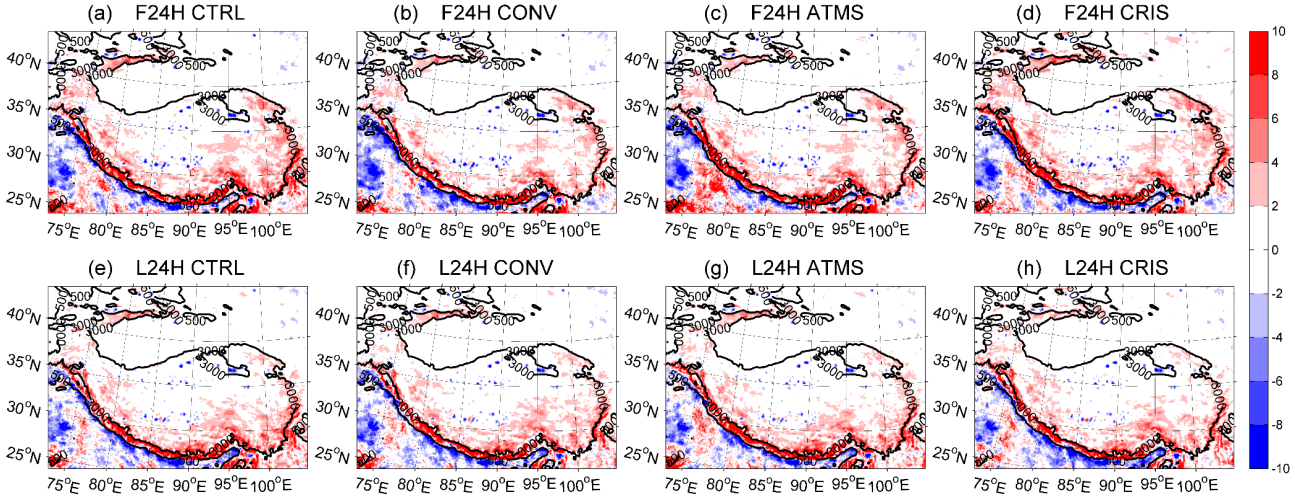

Figure 5. Difference value distribution of monthly mean precipitation (unit: mm) during July for data assimilation minus observation experiments. (a), (e) CTRL minus OBS; (b), (f) CONV minus OBS; (c), (g) ATMS minus OBS for (a)–(d) F24Hforecast and (e)–(h) L24Hforecast. Contours are altitude (unit: m).

Atmos. Meas. Tech. Discuss., doi:10.5194/amt-2017-31, 2017
Manuscript under review for journal Atmos. Meas. Tech.
Discussion started: 27 February 2017

Atmospheric Measurement Techniques Discussions

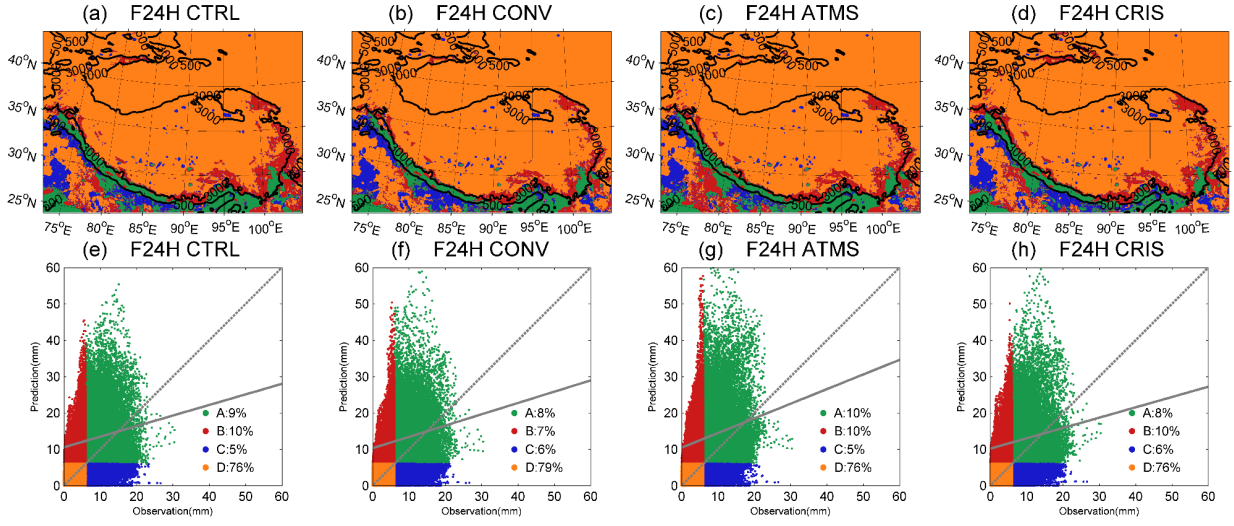

633

634 **Figure 6.** Spatial patterns of (a)–(d) the contingency table and (e)–(h) the scatter plots (monthly mean 24 h rainfall over 6 mm threshold is defined

635 as an "event"). A, B, C and D indicate the Hits, False alarms, Misses and Correct rejections in Table 1, respectively. The solid grey lines indicate

636 the regression line of A. Contours are altitude (unit: m).

637

Atmos. Meas. Tech. Discuss., doi:10.5194/amt-2017-31, 2017
Manuscript under review for journal Atmos. Meas. Tech.
Discussion started: 27 February 2017

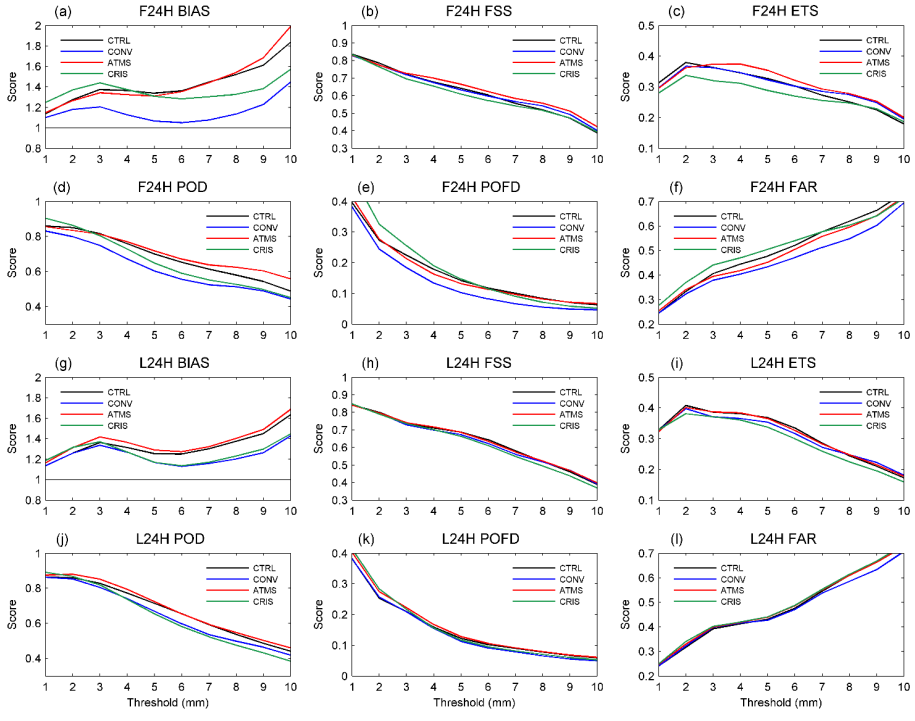

638

639 **Figure 7.** Monthly and domain average validation statistics. (a)–(f) F24H forecast and (g)–(l) L24Hforecast.

Atmos. Meas. Tech. Discuss., doi:10.5194/amt-2017-31, 2017
Manuscript under review for journal Atmos. Meas. Tech.
Discussion started: 27 February 2017

Atmospheric Measurement Techniques Discussions

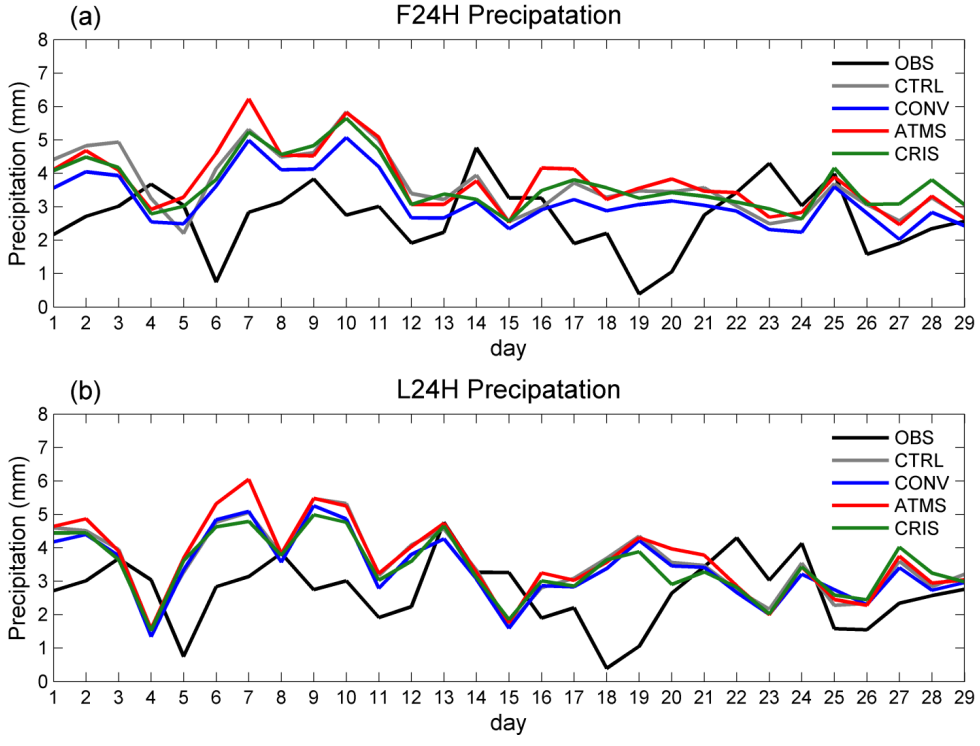

640

641 **Figure 8.** Daily precipitation distribution (unit: mm)

Atmos. Meas. Tech. Discuss., doi:10.5194/amt-2017-31, 2017
Manuscript under review for journal Atmos. Meas. Tech.
Discussion started: 27 February 2017

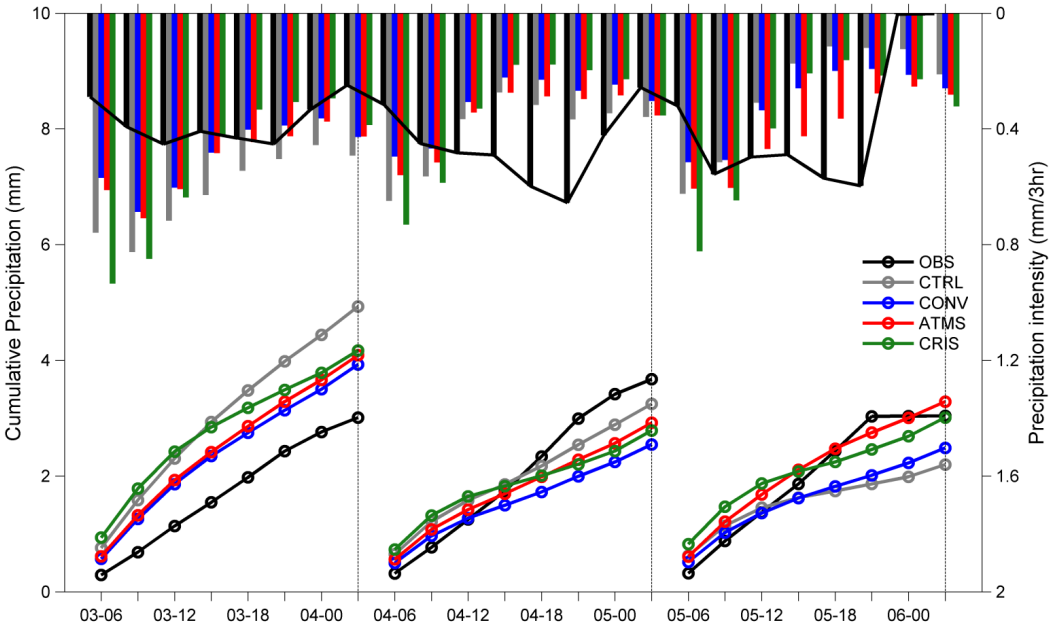

642

643 **Figure 9.** Rainfall intensities (bars) calculated for every 3 h amount of precipitation. The cumulative precipitation (curves) is defined as the

644 precipitation accumulated for each 3 h starting at 06:00 UTC during 3–6 July. The unit is mm.

Atmos. Meas. Tech. Discuss., doi:10.5194/amt-2017-31, 2017
Manuscript under review for journal Atmos. Meas. Tech.
Discussion started: 27 February 2017

Atmospheric Measurement Techniques Discussions

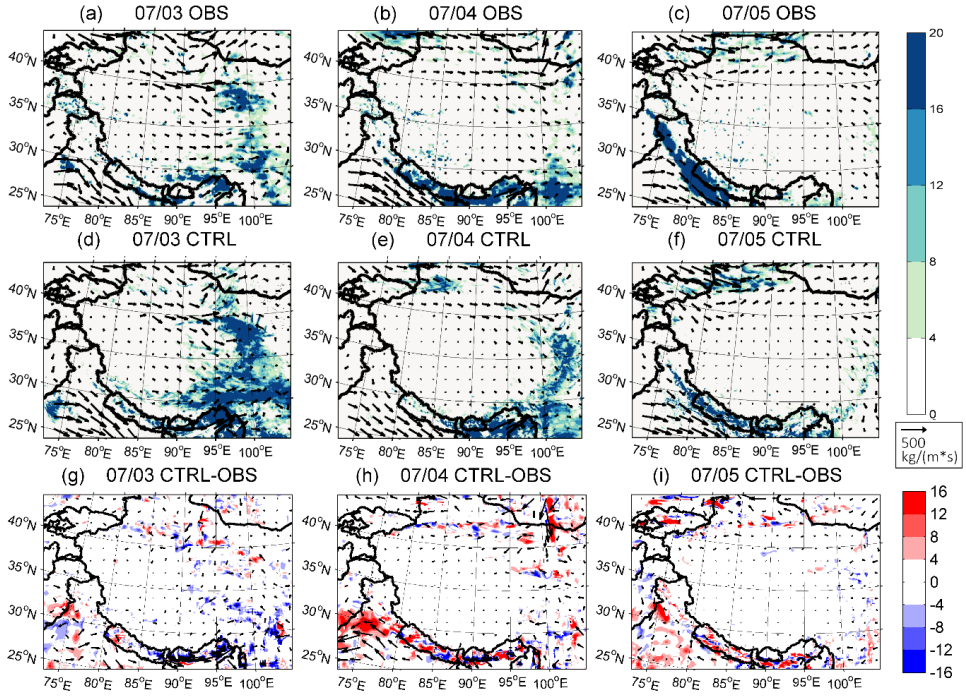

Figure 10. (a)–(f) F24H forecasts of precipitation quantity (shadings) and water vapor flux (vectors) during 3–6 July for (a)–(c) OBS and (d)–(f) CTRL. (g)–(i) Differences in water vapor flux (vectors) and water vapor divergence (shadings) between CTRL and OBS. The unit of precipitation quantity is mm. The units for water vapor flux and divergence is kg/(m*s) and kg/(m2*s), respectively.

Atmos. Meas. Tech. Discuss., doi:10.5194/amt-2017-31, 2017
Manuscript under review for journal Atmos. Meas. Tech.
Discussion started: 27 February 2017

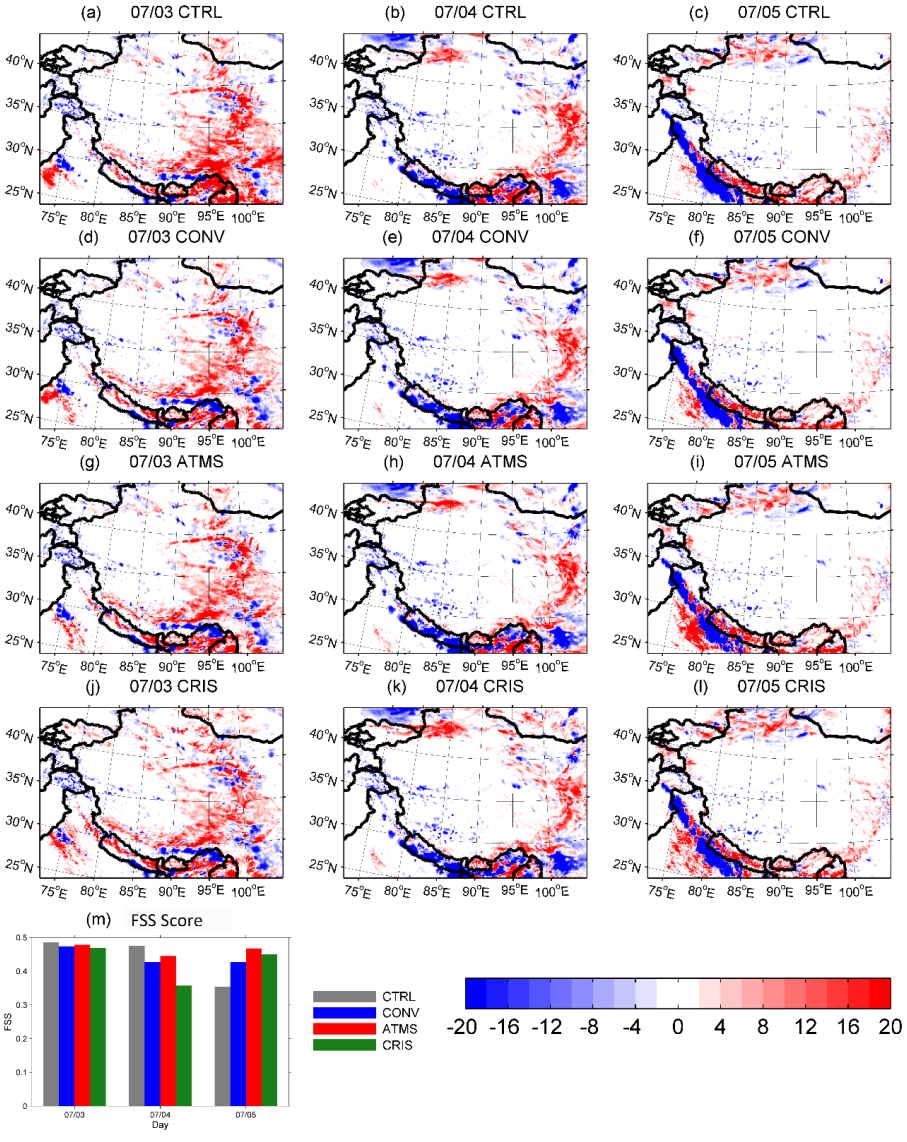

Figure 11. (a)–(l) are Differences between the simulated F24H precipitation and the observed distribution and (m) is the FSS skill scores with 8 mm threshold during 3–6 July. The unit of differences is mm.